

Radiometer Calibration Using Co-located GPS Radio Occultation Measurements

William J. Blackwell, *Senior Member, IEEE*, Rebecca Bishop, Kerri Cahoy, *Member, IEEE*, Brian Cohen, Clayton Crail, Lidia Cucurull, Pratik Dave, Michael DiLiberto, Neal Erickson, Chad Fish, Shu-peng Ho, R. Vincent Leslie, Idahosa A. Osaretin

Abstract—We present a new high-fidelity method of calibrating a cross-track scanning microwave radiometer using Global Positioning System (GPS) radio occultation (RO) measurements. The radiometer and GPSRO receiver periodically observe the same volume of atmosphere near the Earth's limb, and these overlapping measurements are used to calibrate the radiometer. Performance analyses show that absolute calibration accuracy better than 0.25 K is achievable for temperature sounding channels in the 50–60 GHz band for a total-power radiometer using a weakly coupled noise diode for frequent calibration and proximal GPSRO measurements for infrequent (approximately daily) calibration. The method requires GPSRO penetration depth only down to the stratosphere, thus permitting the use of a relatively small GPS antenna. Furthermore, only coarse spacecraft angular knowledge (approximately one degree RMS) is required for the technique, as more precise angular knowledge can be retrieved directly from the combined radiometer and GPSRO data, assuming the radiometer angular sampling is uniform. These features make the technique particularly well-suited for implementation on a low-cost CubeSat hosting both radiometer and GPSRO receiver systems on the same spacecraft. We describe a validation platform for this calibration method, the Microwave Radiometer Technology Acceleration (MiRaTA) CubeSat, currently in development for the NASA Earth Science Technology Office. MiRaTA will fly a multi-band radiometer and the Compact TEC/Atmosphere GPS Sensor (CTAGS) in 2015.

Index Terms—Microwave, remote sensing, temperature, humidity, precipitation, radiometer, calibration, radio occultation, GPSRO, GPS, GNSS, RO-Cal, cubesat, nanosatellite, MiRaTA, CTAGS, MicroMAS, AMSU, ATMS

I. INTRODUCTION

PASSIVE MICROWAVE observations from spaceborne scanning radiometers have proven profoundly useful in a variety of atmospheric applications ranging from mesoscale and synoptic numerical weather prediction to climate study [1].

This work is sponsored by the Assistant Secretary of Defense for Research & Engineering under Air Force Contract FA8721-05-C-0002. Opinions, interpretations, conclusions and recommendations are those of the authors and are not necessarily endorsed by the United States Government.

W. J. Blackwell, C. Crail, M. DiLiberto, R. V. Leslie, and I. A. Osaretin are with the Lincoln Laboratory, Massachusetts Institute of Technology, Lexington, MA 02420 USA (e-mail: wjb@ll.mit.edu).

K. Cahoy, B. Cohen, and P. Dave are with the Department of Aeronautics and Astronautics, Massachusetts Institute of Technology, Cambridge, MA.

L. Cucurull is with the NOAA Earth System Research Laboratory, Boulder, CO.

Shu-peng Ho is with the University Corporation for Atmospheric Research, Boulder, CO

Rebecca Bishop is with the Aerospace Corporation, Redondo Beach, CA
Chad Fish is with the Utah State University Space Dynamics Laboratory, Logan, UT

Neal Erickson is with the University of Massachusetts, Amherst, MA

Temperature sounding channels near 50–60 GHz and water vapor sounding channels near 183.31 GHz penetrate most non-precipitating clouds and thus provide atmospheric profiling capability in almost all weather conditions. In the climate context, measurements of the atmosphere using microwave radiometry have provided a benchmark climate record of temperature trends dating back to the Microwave Sounding Unit (MSU), which began operation in 1979. MSU was followed by the Advanced Microwave Sounding Unit, which began operation in 1998. The Advanced Technology Microwave Sounder (ATMS) is the first in a series of new cross-track scanning sounders developed for the Joint Polar Satellite System (JPSS). ATMS was launched on October 28, 2011 on the Suomi National Polar Partnership satellite.

Absolute calibration of spaceborne microwave scanning instruments for high-fidelity atmospheric research is immensely challenging and nearly impossible to fully trace to a reference standard [2], and bias corrections of up to several degrees Kelvin are routinely used [3]. Problems associated with reflector emissivity and internal calibration target (ICT) contamination have been reported [4]. Previous comparisons of AMSU-A observations that were co-located to COSMIC/FORMOSAT-3 GPSRO observations indicated biases as large as 1.92 K [5].

GPS radio occultation (GPSRO) measurements have also been used extensively to improve weather forecasting and assessments of climate [6], [7]. Temperature profile accuracies approaching 0.1 K are achievable in the upper troposphere and lower stratosphere [8], and recent work has presented techniques for probing down to the boundary layer [9]. GPSRO measurements are inherently well-calibrated due to their fundamental dependence on time delays, which can be traced to NIST standards [5]. However, GPSRO measurements have relatively sparse geospatial coverage. When the COSMIC/FORMOSAT-3 constellation was at peak operational capacity, it provided approximately 2,000 occultation profiles per day, compared with over 3,000,000 soundings per day for ATMS.

In this paper, we explore the combined use of passive microwave sounding and GPSRO observations to leverage the benefits of both in order to achieve highly accurate calibration with dense geospatial sampling. Furthermore, we investigate a new method of two-point calibration, where the traditional calibration points of cold sky and warm ICT are replaced with cold sky and a warm noise diode that is periodically calibrated with GPSRO measurements to eliminate drift [10]. In addition to offering improved calibration, this method also dispenses

with the need for an ICT, which is typically bulky, prone to errors, and often drives the design of the radiometer antenna and scanning system. GPSRO instrumentation, however, is very compact and places no restrictions on the design of the radiometer. In fact, “CubeSat” class spacecraft ($10 \times 10 \times 34$ cm; 4.0 kg) can now accommodate radiometers [11] and GPSRO systems [12] on the same spacecraft, offering a low-cost, high-performance sounding platform.

This paper is organized as follows. First, we provide an overview of the calibration technique (henceforth “RO-Cal”) and describe how it could be implemented on a 50–60 GHz (V-band) radiometer system. We then describe the method in a detailed, step-by-step manner, simulate its performance using the NOAA88b global profile set, and examine the effect of the minimum GPSRO sounding altitude (which drives the required SNR and GPSRO antenna gain requirements) on calibration performance. We then present an end-to-end RO-Cal radiometer calibration simulation. Finally, we describe the Microwave Radiometer Technology Acceleration (MiRaTA) CubeSat that will be used to validate the technique with a launch in 2015.

II. OVERVIEW OF THE RO-CAL METHODOLOGY

The RO-Cal calibration method involves two core operations. First, a quadratic relationship between the GPSRO refractivity profile versus tangent height, $N(h)$, and radiometer brightness temperatures at a particular observing angle and frequency band of interest, $T_B(\theta, f)$, is derived. Second, the radiometer gain, g , (Kelvin/count, where “count” is the output of a 16-bit A/D convertor) is chosen to minimize the residual between the calibrated and GPSRO-derived brightness temperature. Errors due to the quadratic estimation are treated in a weighted least squares sense. In this paper, we consider two cases, one where the angular coincidence between the refractivity profile and the radiometer observations is perfect, for which a closed form expression for g can be derived, and one where there is an unknown scalar angular offset, θ_0 , between the refractivity profile and the radiometer observations, thus requiring a numerical minimization routine to solve for both g and θ_0 . A block diagram summarizing the method components is shown in Fig. 1.

A. Description of the Profile Data and Models Used to Evaluate the RO-Cal Performance

The performance analyses in this paper are all based on simulated observations derived using physical models and global ensembles of atmospheric states. These include the NOAA88b atmospheric profile data set and surface emissivity values, a microwave/millimeter wave non-scattering radiative transfer model, and use of the NOAA88b temperature profiles to generate simulated GPSRO refractivity profiles. The selection of the ensemble of atmospheric states is a critically important part of any simulation study, and we have taken great care to ensure that the profiles included in the analysis are sufficiently representative of a variety of atmospheres that challenge most atmospheric sounding systems.

1) *The NOAA88b Atmospheric Profile Data Set*: The NOAA88b radiosonde/rocketsonde data set contains global profiles that are distributed seasonally and geographically. For this study, 1,000 profiles were randomly chosen from the 7,547 available profiles to allow all of the spectral and spatial convolution operations performed on the data to be executed in several days. Atmospheric temperature, moisture, and ozone are given at 100 discrete levels from the surface to altitudes exceeding 50 km. Skin surface temperature is also recorded. Additional details on the geographic representation of the profiles and the profile variability can be found in [13].

2) *Microwave Surface Emissivity*: Surface emissivity values from the NOAA88b data set were used. These include land and ocean emissivities and range from 0.5 to 0.6 over ocean and from 0.7 to 0.98 over land. We note that surface emissivity is a relatively weak contributor to brightness temperature for the frequencies and viewing angles considered in this study (a key feature of the method, because interference due to surface emissivity uncertainty is minimized).

3) *Microwave/Millimeter-Wave Non-Scattering Radiative Transfer Models*: Simulated brightness temperature observations for atmospheric profiles in the NOAA88b data set were calculated using the TBARRAY software package of Rosenkranz [14], which was modified to introduce spherical symmetry and accommodate radiative transfer calculations through the Earth’s limb. TBARRAY is a line-by-line routine based on the Liebe Millimeter-wave Propagation Model (MPM) [15], [16]. Scattering was not modeled because cloud liquid water content is not recorded in the NOAA88b data set. This is not a consideration in this work because scattering effects can be flagged by the calibration algorithm (see Section IV-B). The spectral passbands were modeled as boxcar functions using approximately ten discrete frequencies per passband.

4) *GPS Radio Occultation*: GPSRO receivers on low-Earth orbiting (LEO) satellites receive radio frequency signals from higher-altitude GPS satellites. As the LEO satellite and its GPSRO receiver drops behind Earth’s limb from the perspective of the GPS satellite (an ingress occultation), the signal penetrates through the atmosphere from space down to the surface; rising occultations are also used. The path of the signal is affected as it passes through the refractivity gradient of the atmosphere, and results in a measurable frequency deviation in the received signal. The GPS radio frequency signals are traceable to NIST standards (the SI second) with a high degree of accuracy using monitoring and corrections from a series of atomic clocks. The frequency measurement and knowledge of the geometry, in addition to assumptions of spherical symmetry, yield a profile of refractivity as a function of altitude (geometric height) $N(h)$, from which temperature and pressure can be derived when water vapor is negligible. [8], [17], [18], [5], [19].

Refractivity (N) is defined in terms of refractive index n as:

$$N = (n - 1) \cdot 10^6 \quad (1)$$

In Earth’s neutral atmosphere, refractivity is approximately related to the pressure (P), the temperature (T) and the partial

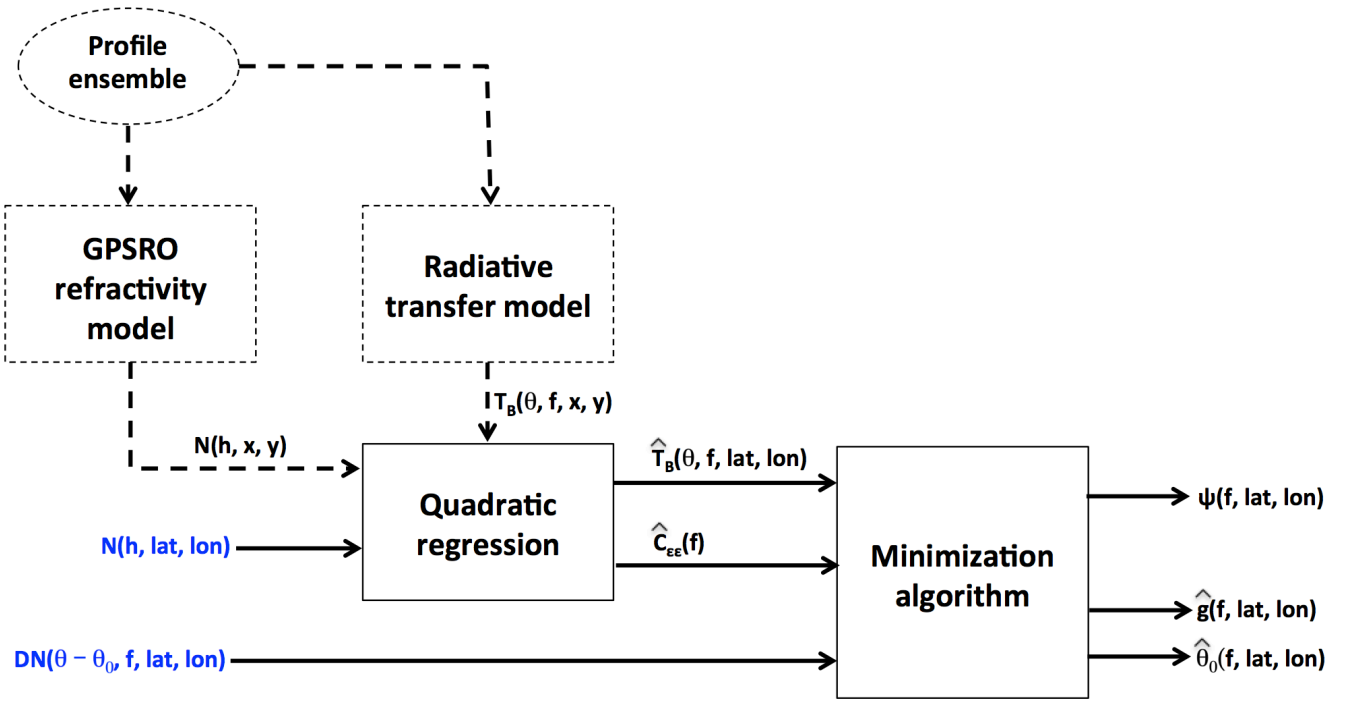


Fig. 1. Block diagram of the GPSRO microwave radiometer calibration procedure. Dashed lines indicate operators that are trained off-line using ensemble data sets (NOAA88b in this case). The inputs to the algorithm are radiometer counts (digital numbers, DN) and the refractivity profile, $N(h)$. Outputs are the estimated radiometer gain, g , and the estimated angular error in the radiometer scan plane, θ_0 .

pressure of water vapor (P_W) by the following equation [20]:

$$N = 77.6 \frac{P}{T} + 3.73 \times 10^5 \frac{P_W}{T^2} \quad (2)$$

We note that a more accurate relationship is given in [21], but the simple relationship above is used here. In this study, the NOAA88b temperature and water vapor profiles, defined at fixed pressure levels, are used with (2) to generate refractivity as a function of pressure. Note that at lower altitudes in moist tropical regions, the estimated GPSRO refractivity may significantly depend on the moisture distribution. In the upper troposphere and stratosphere where moisture is negligible, the refractivity noise in the fractional refractivity can be as small as 0.2% (see Fig. 13 in [8]). Currently, multi-year GPSRO data can be obtained from six different RO centers (see [19] for details). By using the differences and standard deviations of the individual centers relative to the inter-center mean to quantify the structural uncertainty, it was confirmed that the mean refractivity anomalies among centers agree within 0.01% with a standard deviation 0.2% (Table 2 in [19]). In this study, we add a random refractivity noise commensurate with that reported by [8] in the calculated refractivity.

III. ESTIMATION OF RADIOMETER BRIGHTNESS TEMPERATURE FROM GPSRO REFRACTIVITY

The first step of the calibration algorithm involves a quadratic regression on the GPSRO refractivity profile, $N(h)$, to estimate the radiometer brightness temperature as a function of scan angle through the Earth's limb, $T_B(\theta, f)$. It is assumed that the radiometer is sampled such that there is a uniform 0.1-degree spacing between the limb observations.

A. Radiometer Assumptions

For the simulations in this paper, we consider six channels in the 50–60 GHz temperature sounding band (also denoted “V-band”), three channels in the 183.31 GHz water vapor sounding band, and one channel at 206.4–208.4 for cloud ice sensing. The latter four channels are also denoted “G-band”. Channel passbands are given in Table I, and weighting functions for the temperature channels are shown in Fig. 2. These channels closely approximate similar channels on ATMS, with the exception of the 207.4 GHz channel, which is added for consideration in this study. A spacecraft altitude of 400 km is assumed, corresponding closely to the expected initial orbit altitude of MiRaTA (see Section V). The antenna beamwidth is 5.0 degrees (full width at half maximum, FWHM) at 50 GHz and 1.25 degrees FWHM at 200 GHz. Gaussian beam shapes are assumed in the spatial convolution operators. A receiver temperature of 300 K was assumed for the V-band channels; 1000 K was assumed for the G-band channels. A scan rate of one revolution per second was assumed. At 0.1-degree angular spacing, the integration time for each observation is therefore approximately 275 μ sec. A 20-point triangular filter was used to reduce sensor noise in the calibration, as similar filters have been used operationally with ATMS. With these assumptions, typical radiometer sensitivity (RMS noise-equivalent delta temperature, NEDT) values range from 0.2 K (3 K scene) to 0.3 K (250 K scene) for the V-band channels and range from 0.35 K (5 K scene and 200 MHz bandwidth) to 1.1 K (250 K scene and 500 MHz bandwidth) for the G-band channels.

The mean brightness temperatures for the NOAA88b set

TABLE I
SPECTRAL CHARACTERISTICS OF THE RADIOMETER CHANNELS
CONSIDERED IN THIS STUDY.

Channel #	Center Frequency (GHz)	Bandwidth (MHz)
1	52.85	600
2	53.50	600
3	54.15	600
4	54.75	600
5	55.35	600
6	56.65	600
10	183.31 ± 1	500
11	183.31 ± 3	1000
12	183.31 ± 7	2000
13	207.4	2000

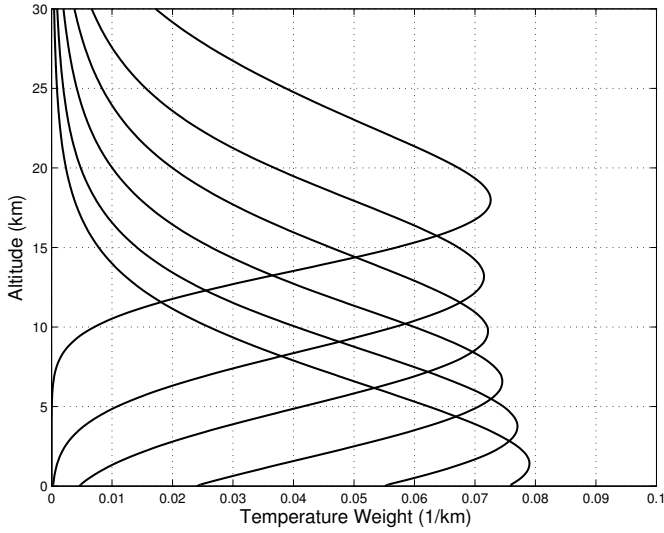


Fig. 2. Temperature weighting functions for the V-band channels considered in this study at nadir incidence over a non-reflective surface. The US 1976 standard atmosphere was used for the calculations.

plotted as a function of sensor scan angle are shown in Fig. 3 for the viewing geometry assumptions described above. The “limb” portion of the Earth’s atmosphere occurs over a range of angles centered at approximately 71 degrees. It should be noted that the Rayleigh-Jeans approximation cannot be used for temperatures below approximately 150 K, and spectral radiance intensities must be evaluated directly using the Planck function.

B. Results

Brightness temperature retrieval performance results for the V-band temperature channels as a function of scene temperature are shown in Fig. 4, and results for the G-band channels are shown in Fig. 5. The sensitivity to GPSRO penetration depth is also shown – the less transparent (more opaque) channels are relatively insensitive to penetration depth, while the more transparent (less opaque) channels are highly sensitive to penetration depth. Retrieval errors of 0.5 K or less are evident for the more opaque V-band channels and degrade by several degrees for the less opaque V-band channels. Errors for the G-band channels range from approximately 1 K to 4 K.

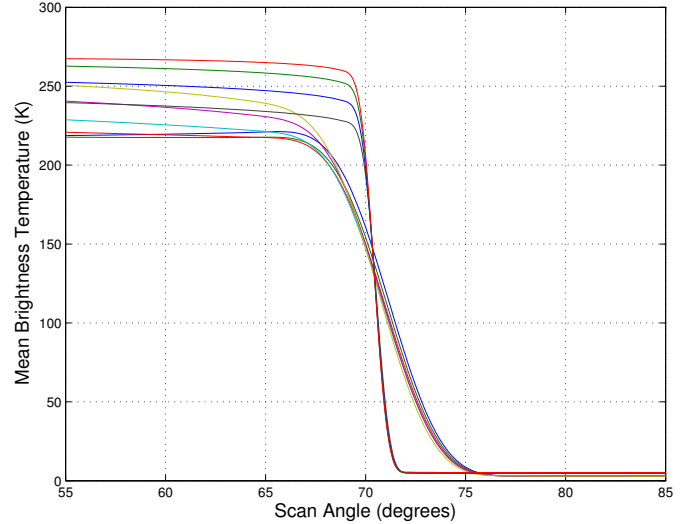


Fig. 3. The mean brightness temperatures calculated for the NOAA88b data set are shown for each of the ten channels considered in this study. The V-band channels (with 5.0-degree FWHM antenna beamwidth) and G-band (with 1.25-degree FWHM antenna beamwidth) are shown. The G-band brightness temperature curves are characterized by a steeper slope due to their narrower antenna beamwidth.

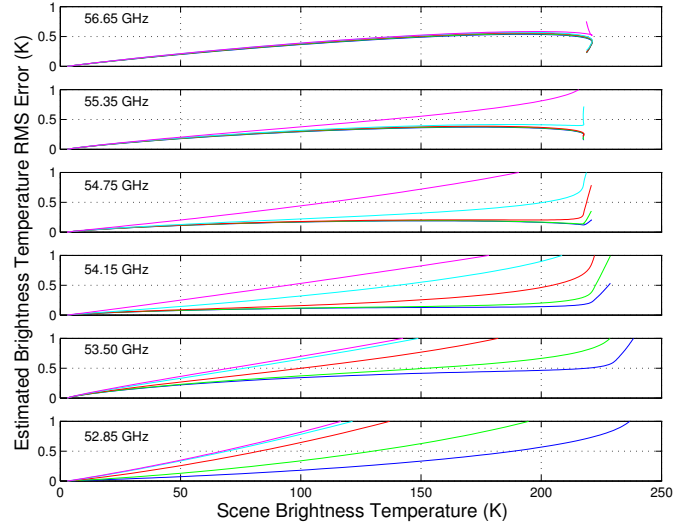


Fig. 4. RMS error for the retrieval of V-band brightness temperature from GPSRO refractivity profiles. Each set of five lines indicates GPSRO penetration depths of 8, 10, 12, 16, and 20 km, with 8 km yielding the lowest errors and 20 km yielding the highest errors in all cases.

The retrieval error $\epsilon(\theta, f) = T_B(\theta, f) - \hat{T}_B(\theta, f)$ for each channel is characterized by an error covariance matrix, $C_{\epsilon\epsilon}(f)$, where each row and column is associated with a single radiometer view angle. This error covariance will be used in the subsequent minimization routine to estimate the radiometer gain, g .

IV. ESTIMATION OF RADIOMETER GAIN

The second component of the RO-Cal algorithm uses the retrieved brightness temperatures, $\hat{T}_B(\theta, f)$ as a temperature reference from which radiometer gain, g , is derived. If there is

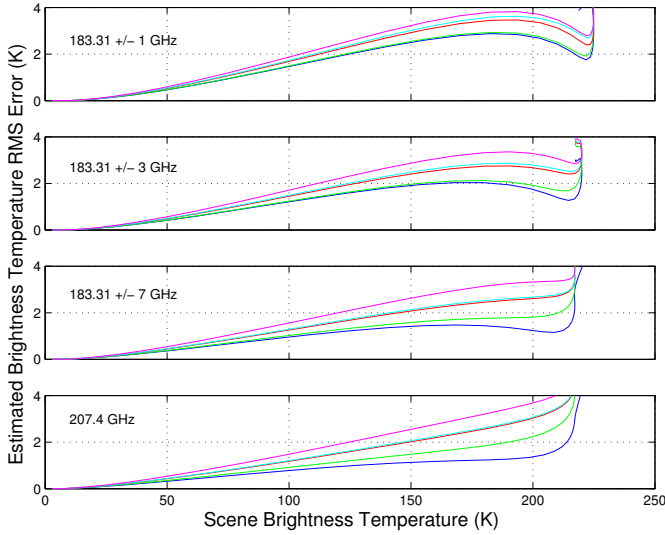


Fig. 5. RMS error for the retrieval of G-band brightness temperature from GPSRO refractivity profiles. Each set of five lines indicates GPSRO penetration depths of 8, 10, 12, 16, and 20 km, with 8 km yielding the lowest errors and 20 km yielding the highest errors in all cases.

no angular offset between the retrieved and actual brightness temperatures, a closed form solution can be derived for g using weighted least squares. The cost function to be minimized (for each channel) is:

$$\Psi = (\hat{\mathbf{T}}_B - \tilde{\mathbf{T}}_B)' \mathbf{C}_{\epsilon\epsilon}^{-1} (\hat{\mathbf{T}}_B - \tilde{\mathbf{T}}_B) \quad (3)$$

We have used boldface type to indicate that angular dependence has been captured as elements in vectors or matrices, and $\tilde{\mathbf{T}}_B$ is the calibrated radiometer brightness temperature defined as follows:

$$\tilde{\mathbf{T}}_B = g(\mathbf{DN} - \mathbf{DN}_c) + T_c \quad (4)$$

where \mathbf{DN} is the radiometer count output (digital number) when viewing the limb, \mathbf{DN}_c is the radiometer output when viewing cold sky, and T_c is the cold sky brightness temperature.

For the simulations presented below, radiometer gain (Kelvin/count) for each profile was assigned a Gaussian random value with mean 0.02 and standard deviation 0.0012, which is representative of radiometer behavior at the frequencies of interest in this study. For cases with a non-zero angular offset θ_0 between $\hat{\mathbf{T}}_B$ and $\tilde{\mathbf{T}}_B$, a Gaussian random value was assigned to θ_0 with mean of zero and standard deviation of one, which is representative of current commercially available CubeSat attitude and determination systems. Approximately 200 scan angles ranging from 55 to 75 degrees were used for the V-band calibrations, and approximately 40 scan angles ranging from 67 to 71 degrees were used for the G-band calibrations.

A. Case I: No Angular Offset

If there is no angular offset between $\hat{\mathbf{T}}_B$ and $\tilde{\mathbf{T}}_B$, then \hat{g} can be expressed in closed form as:

$$\hat{g} = \frac{(\hat{\mathbf{T}}_B - T_c)' \mathbf{C}_{\epsilon\epsilon}^{-1} (\mathbf{DN} - \mathbf{DN}_c)}{(\mathbf{DN} - \mathbf{DN}_c)' \mathbf{C}_{\epsilon\epsilon}^{-1} (\mathbf{DN} - \mathbf{DN}_c)} \quad (5)$$

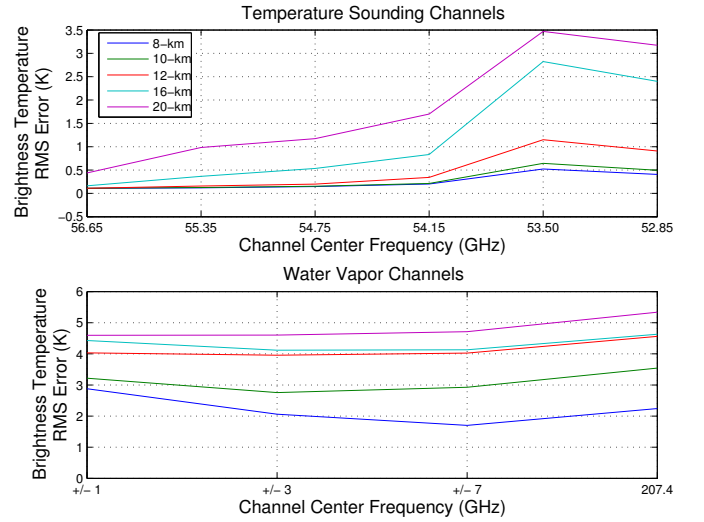


Fig. 6. RMS error for calibrated brightness temperature for a 300 K scene assuming perfect angle knowledge. The G-band channel center frequencies in the lower panel are 183.31 ± 1 , 183.31 ± 3 , 183.31 ± 7 , and 206.4 – 208.4 GHz.

The RMS calibration errors for this case are shown in Fig. 6 when calibrating a 300 K scene. The V-band performance is excellent (approximately 100 mK) for opaque channels with GPSRO penetration depths down to 12 km, and performance degrades with decreasing penetration depth, markedly so for non-opaque channels. G-band calibration performance is not as good, with errors of several degrees Kelvin.

B. Case II: Constant Angular Offset

We now examine a case with an unknown but constant angular offset, θ_0 between $\hat{\mathbf{T}}_B$ and $\tilde{\mathbf{T}}_B$. Now, a more sophisticated method is needed to minimize (3) because the radiometer gain and offset angle must be jointly optimized. We define a “shifted” $\tilde{\mathbf{T}}_B$, $\tilde{\mathbf{T}}_B^S$, such that $\tilde{\mathbf{T}}_B^S = \tilde{\mathbf{T}}_B(\theta - \theta_0)$, and a new cost function is minimized:

$$\Psi = (\hat{\mathbf{T}}_B - \tilde{\mathbf{T}}_B^S)' \mathbf{C}_{\epsilon\epsilon}^{-1} (\hat{\mathbf{T}}_B - \tilde{\mathbf{T}}_B^S) \quad (6)$$

The Nelder–Mead Simplex method [22] was used to numerically minimize (6) given $\hat{\mathbf{T}}_B$ and initial guesses for radiometer gain and offset angle. The parameter mean values were used for the initial guesses, as frequent noise diode calibrations should produce \hat{g} estimates within a fraction of a percent of true values [10].

A very useful diagnostic is the value of the cost function (6) after minimization, as this can be used for quality control of the estimated values. We declare a “failure to converge” condition if the cost function exceeds 200 (the number of angles used) for the V-band channels and 40 (the number of angles used) for the G-band channels. The percentage of successful calibrations is shown in Fig. 7. Opaque channels are almost always successfully calibrated, although the success rate drops to approximately 75% for the G-band channels.

The RMS calibration errors for this case are shown in Fig. 8 when calibrating a 300 K scene. V-band performance is still very good, degrading to approximately 0.25 K for the

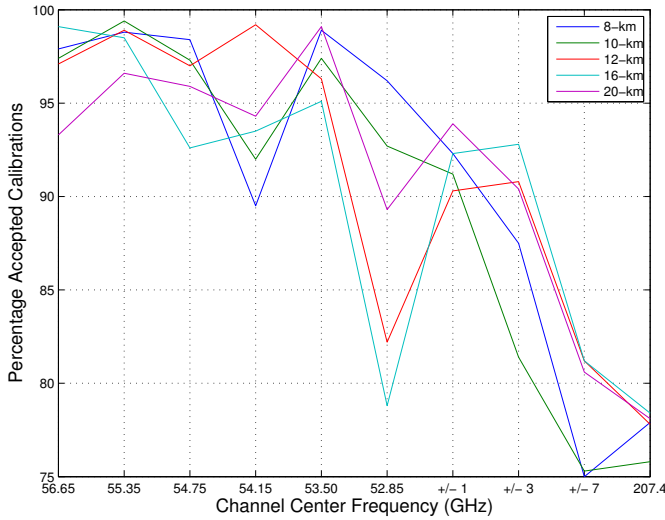


Fig. 7. Percentage of successful calibrations. The G-band channel center frequencies in the lower panel are 183.31 ± 1 , 183.31 ± 3 , 183.31 ± 7 , and 206.4–208.4 GHz.

opaque channels for GPS penetration depths down to 12 km, and performance degrades with decreasing penetration depth, markedly so for non-opaque channels. G-band calibration performance is not as good, with errors exceeding four degrees Kelvin.

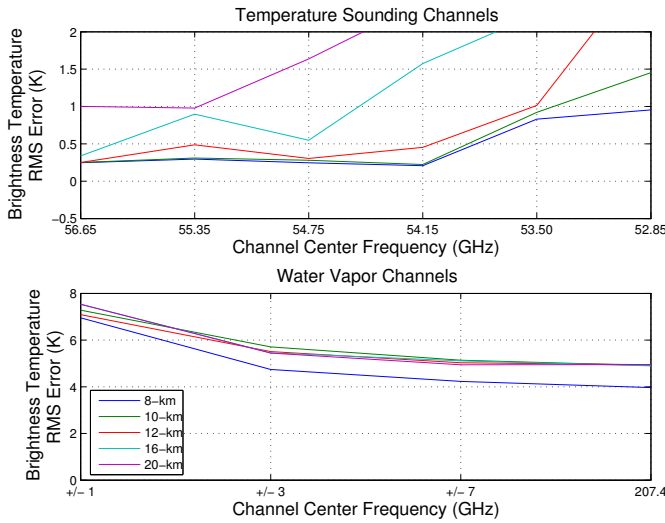


Fig. 8. RMS error for calibrated brightness temperature for a 300 K scene with angle offset retrieved from observations. The G-band channel center frequencies in the lower panel are 183.31 ± 1 , 183.31 ± 3 , 183.31 ± 7 , and 206.4–208.4 GHz.

The locations of the rejected calibrations were examined for evidence of any geographically problematic regions. The locations of all 1000 profiles and the rejected calibrations for the 207.4-GHz channel with a 20-km GPSRO penetration depth (the worst performing case) is shown in Fig. 9. The locations of rejected cases are uniformly distributed around the globe with no obvious geographical correlations.

The angular offsets were also retrieved as part of the calibration process. The angle retrieval RMS error is shown

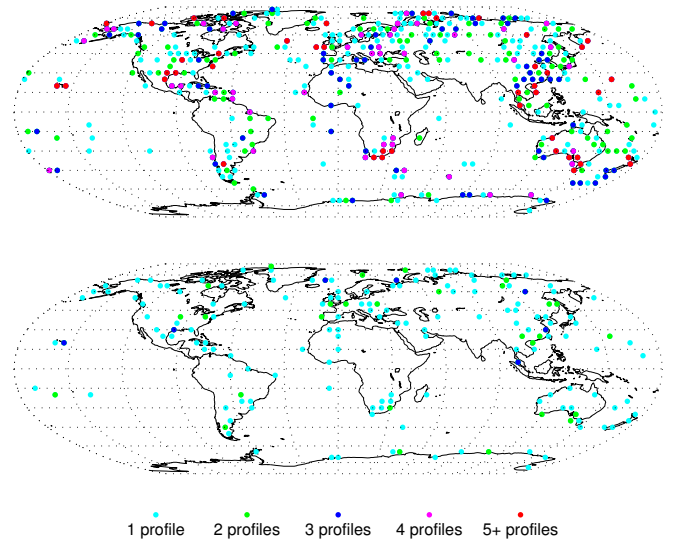


Fig. 9. The locations of all 1000 profiles used in this study are shown in the top panel, and the locations of the rejected calibrations for the 207.4-GHz channel with a 20-km GPSRO penetration depth (worst case) are shown in the bottom panel.

in Fig. 10. The results are quite good, as accuracies better than 0.005 degrees (approximately 85 microradians or 18 arcseconds) are achieved for opaque channels. This level of pointing knowledge (in the sensor scan plane) is commensurate with that achievable with star tracking systems.

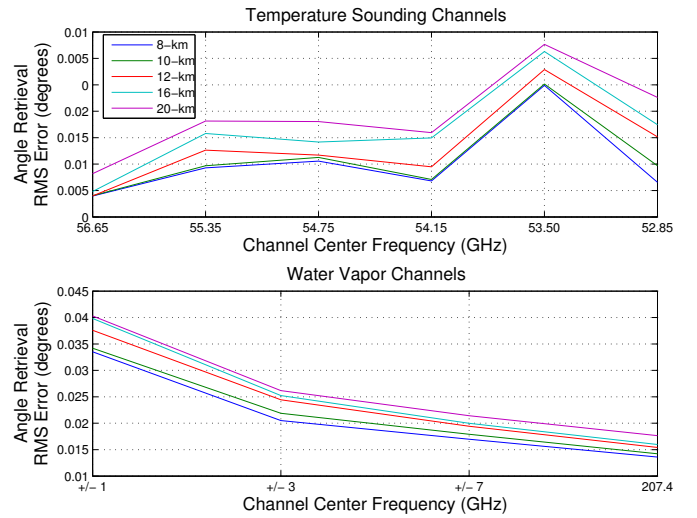


Fig. 10. RMS error for angle offsets retrieved from observations using the RO-Cal algorithm.

C. Discussion

The trend of decreasing calibration error with increasing V-band channel opacity evident in Figures 6 and 8 suggests that further performance improvements could be gained by the addition of more opaque channels. For example, a channel centered near 58.4 GHz with similar bandwidths to those considered in this study would peak near 25 km. If noise

diode drift is highly correlated within the frequency pass-band of the diode, only a single calibration point using an opaque channel would be needed, thereby permitting GPSRO penetration depths down only to the stratosphere. This could be accomplished with a relatively small GPSRO antenna compatible with CubeSat implementation. We note that the G-band channels are not easily calibrated with this technique due primarily to water vapor variability to which the GPSRO measurements are largely blind. Possible enhancements that might improve performance include more sophisticated estimators for \hat{T}_B , inclusion of additional atmospheric data from radiosondes or numerical weather prediction fields, inclusion of channels with more opacity, and treatment of channels simultaneously instead of individually. We also suggest the use of radio occultation with frequencies capable of measuring water vapor.

V. FUTURE VALIDATION OF THE METHODOLOGY WITH THE MIRA TA SPACECRAFT

The RO-Cal methodology is particularly appealing for nanosatellite sounders, which 1) typically have relatively simple attitude determination systems capable of pointing knowledge on the order of a degree, and 2) are severely volume and mass constrained, precluding the use of blackbody internal calibration targets. In this section we briefly describe how the RO-Cal technique will be validated as part of the Microwave Radiometer Technology Acceleration (MiRaTA) CubeSat mission scheduled for launch in 2015 into an orbit with 390 km initial altitude and 52-degree inclination. The MiRaTA CubeSat will carry out the mission objectives over a 90-day mission, including the on-orbit checkout and validation period. MiRaTA is a 3U CubeSat comprising V- and G-band radiometers (52-58 GHz, 175-191 GHz, and 206.4-208.4 GHz), the Compact TEC/Atmosphere GPS Sensor (CTAGS) with five-element patch antenna array, and relatively standard CubeSat spacecraft subsystems for attitude determination and control, communications, power, and thermal control. The spacecraft dimensions are $10 \times 10 \times 34$ cm, total mass is 4.0 kg, and total average power consumption is 6W.

A. Concept of Operations

The primary MiRaTA mission concept of operations (ConOps) is summarized in Fig. 11. The MiRaTA spacecraft will perform a slow pitch up/down maneuver once per orbit to permit the radiometer and GPSRO observations to sound overlapping volumes of atmosphere through the Earth's limb, where sensitivity, calibration, and dynamic range are optimal. These observations will be compared to radiosondes, global high-resolution analysis fields, other satellite observations (for example, ATMS and the Cross-track Infrared Sounder on the Suomi NPP satellite) and with each other (GPSRO and radiometer) using radiative transfer models.

B. Spacecraft Overview

The MiRaTA spacecraft is shown in Fig. 12. There are no moving mechanisms and the only deployable structures

(both with flight heritage) are two solar panels and a simple tape-spring antenna for UHF communications with the NASA Wallops Flight Facility 18.3-m ground station. The radiometers view the Earth through the nadir deck of the spacecraft, and in this frame, the GPSRO patch antennas have a field of view in the zenith direction, which is oriented to the limb during GPSRO sounding via a simple pitch or roll maneuver (see Fig. 11). A separate GPS antenna is used for precision orbit determination during the maneuver. The radiometer and GPSRO fields of view are used to probe the same volume of atmosphere by using the control authority of the reaction wheel assembly to rotate the spacecraft about either the pitch or roll axes approximately once per orbit.

The MiRaTA CubeSat will contain two complete instrument systems, a tri-band atmospheric sounder and CTAGS, which is based on work described in [12]. These two instruments will be operated in a manner to allow cross-comparison and cross-calibration. The tri-band microwave atmospheric sounder provides co-located observations over three frequency bands, 52-58 GHz, 175-191 GHz, and 206.4-208.4 GHz and comprises two radiometer subsystems: 1) V-band (52-58 GHz) front-end receiver with weakly coupled noise diode, low-noise MMIC amplifier, mixer, intermediate frequency (IF) preamplifier, and ultracompact IF spectrometer with highly-scalable LTCC/SIW architecture operating over the 23-29 GHz IF band to provide six channels with temperature weighting functions approximately uniformly distributed over the troposphere and lower stratosphere (see Fig. 2); and 2) broadband G-band mixer front end operating from 175.31 to 208.4 GHz with a conventional IF spectrometer with lumped element filters. Approximately 1,000 GPSRO+radiometer Earth limb scans are expected over the course of the mission.

VI. SUMMARY AND FUTURE WORK

We have presented a new radiometer calibration method that uses frequent observations of noise diodes and infrequent GPSRO measurements to calibrate any drift in the noise diode output. This method offers improved accuracy relative to traditional methods while being easier to accommodate on very small spacecraft with coarse attitude determination capabilities. Simulation analyses indicate that absolute accuracies approaching 0.25 K are obtainable for opaque V-band channels. If diode drift is highly correlated with frequency, this calibration can be readily transferred to non-opaque channels. The MiRaTA CubeSat mission is in development to validate the simulation results presented here, and a launch is expected in 2015.

We suggest a number of items to pursue as future work. First, no effort has been made here to optimize the channel sets for best calibration algorithm performance. Channels with additional opacity should be considered. Second, algorithm sensitivity analyses could be performed with respect to antenna beamwidth, pointing accuracy/jitter, sensor noise, radiometer sample rate (angular spacing), and orbital characteristics. Third, the radiative transfer simulations can be improved by removing the constraint of spherical homogeneity. This could be done by considering multiple profiles along the line of

Nominal Sci Ops for Coupled Atmospheric GPSRO & Microwave Radiometry

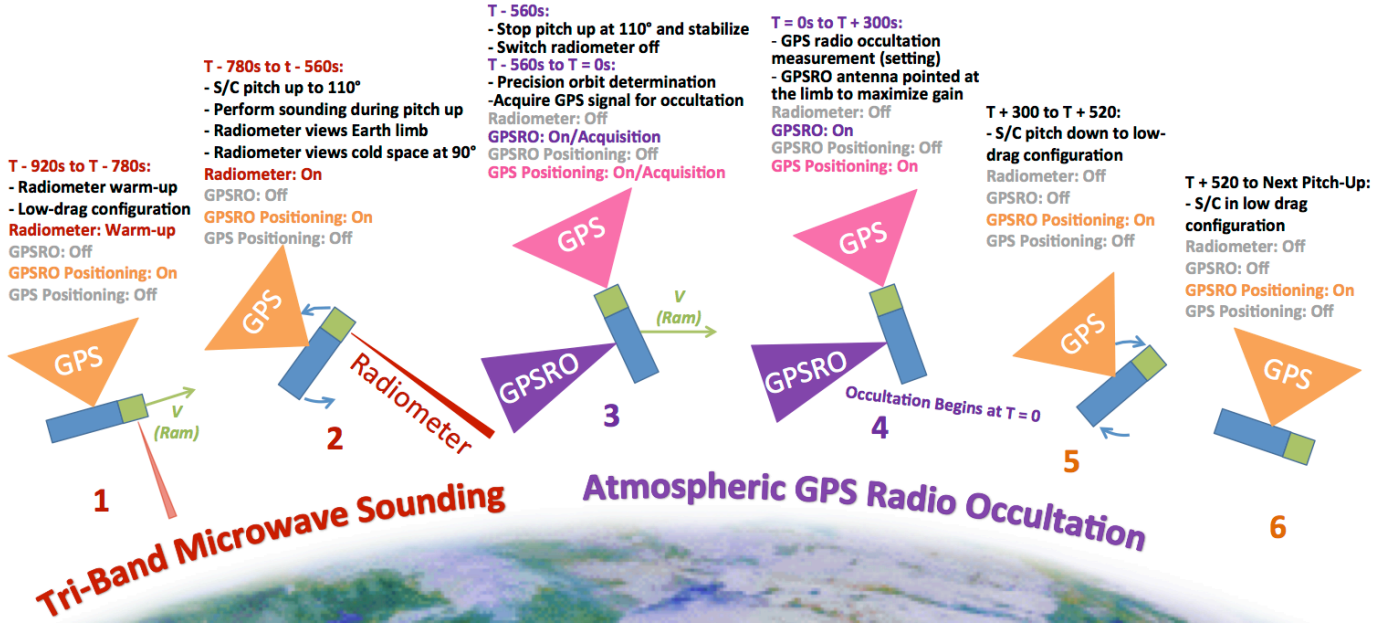


Fig. 11. The MiRaTA primary mission validation concept of operations (ConOps) is shown above. A slow pitch maneuver ($0.5^\circ/\text{sec}$) is used to scan the radiometer field of view through the Earth's limb and subsequently direct the GPSRO field of view through the same atmosphere to catch a setting occultation. The entire maneuver takes about 20 minutes.

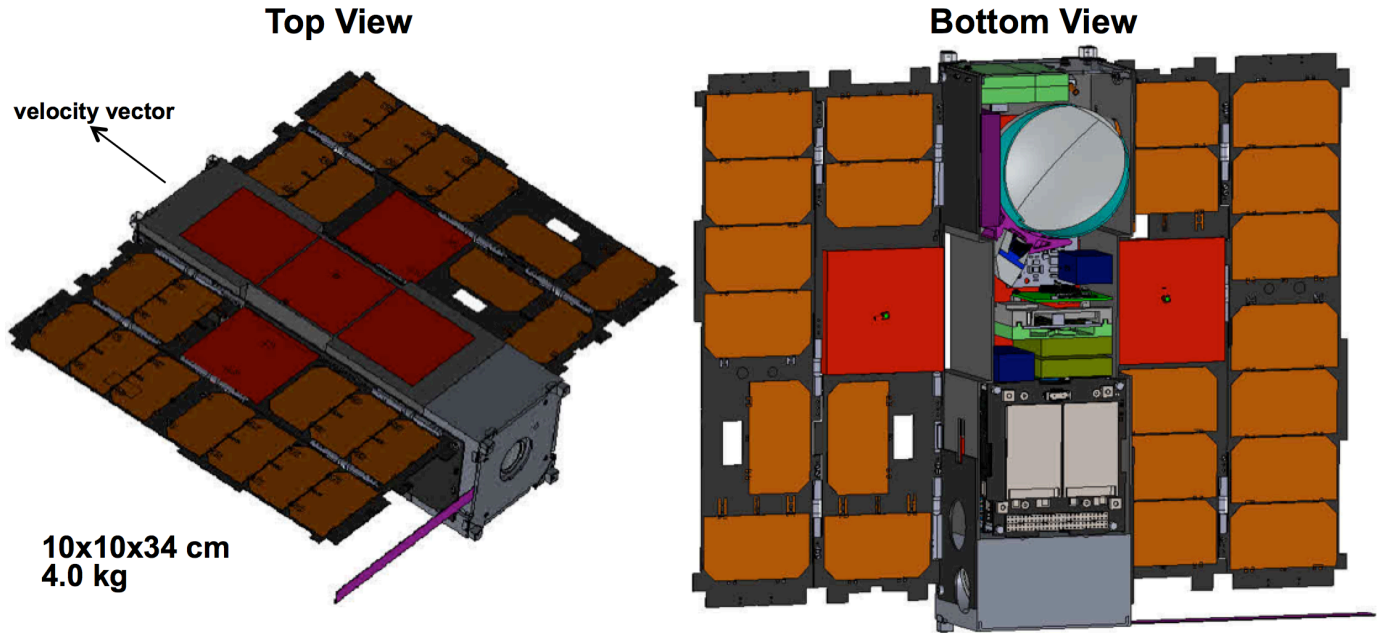


Fig. 12. A view looking down onto the top of the MiRaTA spacecraft is shown on the left, and a view of the bottom of the spacecraft (with the bottom body panel removed for illustration) is shown on the right. The five-element antenna patch array on the zenith deck of the spacecraft is used for the atmospheric GPSRO measurements. The side patches are integrated onto deployable solar panels (mounted beneath the substrate) for simplicity and reliability. The primary spacecraft components are visible in the image on the right, including (from the bottom up): three-axis reaction wheel assembly, avionics and power stack (batteries visible), GPS receivers (two), and radiometer components. The side patch antennas fold inwards and occupy a fraction of space along the body panels of the spacecraft prior to deployment. The holes in the deployed solar panels allow access to spacecraft electronics. A representative UHF tape-spring antenna is shown for illustration purposes - the flight version will likely be positioned on the lower deck of the spacecraft to permit the use of a larger ground plane.

sight, as is done in [23]. Fourth, the minimization routines could be executed using all channels instead of each channel

individually. This could be accommodated, for example, by using 1DVAR minimization with *a priori* constraints on the

gain and offset angle that are derived from pre-launch characterizations. Finally, we suggest analysis of any microwave sounder data collected during a spacecraft maneuver that might be serendipitously co-located with operational GPSRO observations.

ACKNOWLEDGMENTS

We gratefully acknowledge many helpful conversations with Prof. Jose Martinez (Northeastern University) on the MiRaTA antenna design, Prof. Eric Miller (Tufts University) on limb data processing, and the MicroMAS team at MIT Space Systems Laboratory.

REFERENCES

- [1] M. A. Janssen, "An introduction to the passive microwave remote sensing of atmospheres," in *Atmospheric Remote Sensing by Microwave Radiometry*, M. A. Janssen, Ed. New York: Wiley, 1993, ch. 1.
- [2] A. Wallard and W. Zhang, *Measurement Challenges for Global Observation Systems for Climate Change Monitoring: Traceability, Stability and Uncertainty*. WMO/TD-No. 1557: IOM-Report No. 105, 2010.
- [3] T. Mo, "Cross-Scan Asymmetry of AMSU-A Window Channels: Characterization, Correction, and Verification," *IEEE Trans. Geosci. Remote Sens.*, vol. 51, no. 3, pp. 1514–1530, Mar. 2013.
- [4] D. B. Kunkee, G. A. Poe, S. D. Swadley, Y. Hong, and M. Werner, "Special Sensor Microwave Imager Sounder (SSMIS) Radiometric Calibration Anomalies Part I: Identification and Characterization," *IEEE Trans. Geosci. Remote Sens.*, vol. 46, no. 4, pp. 1017–1033, April 2008.
- [5] S.-P. Ho, W. Schreiner, and X. Zhou, "Using SI-traceable Global Positioning System radio occultation measurements for climate monitoring," *Bull. Amer. Meteor. Soc.*, no. 7, pp. S36–S37, 2009.
- [6] L. Cucurull, "Improvement in the Use of an Operational Constellation of GPS Radio Occultation Receivers in Weather Forecasting," *Wea. Forecasting*, 2010.
- [7] L. Cucurull, J. C. Derber, and R. J. Purser, "A bending angle forward operator for global positioning system radio occultation measurements," *J. Geophys. Res.*, no. D18111, 2013.
- [8] E. R. Kursinski, G. A. Hajj, J. T. Schofield, R. P. Linfield, and K. R. Hardy, "Observing Earth's atmosphere with radio occultation measurements using the Global Positioning System," *J. Geophys. Res.*, vol. 102, pp. 23 429–23 465, Jul. 1997.
- [9] C. O. Ao, G. A. Hajj, T. K. Meehan, D. Dong, B. A. Iijima, A. J. Mannucci, and E. R. Kursinski, "Rising and setting GPS occultations by use of open-loop tracking," *J. Geophys. Res.*, 2009.
- [10] S. T. Brown, S. Desai, W. Lu, and A. B. Tanner, "On the long-term stability of microwave radiometers using noise diodes for calibration," *IEEE Trans. Geosci. and Remote Sens.*, no. 7, pp. 1908–1920, July 2007.
- [11] W. J. Blackwell, et al., "Nanosatellites for earth environmental monitoring: The MicroMAS project," *Proc. 26th Ann. AIAA/USU Conf. Small Sat., SSC12-XI-2*, Aug. 2012.
- [12] R. L. Bishop, D. A. Hinkley, D. R. Stoffel, D. E. Ping, P. R. Straus, and T. R. Brubaker, "First Results From the GPS Compact Total Electron Content Sensor (CTECS) on the PSSC2 Nanosat," *Proc. 26th Ann. AIAA/USU Conf. Small Sat., SSC12-XI-2*, Aug. 2012.
- [13] W. Blackwell, L. Bickmeier, R. Leslie, M. Pieper, J. Samra, C. Surravadee, and C. Upham, "Hyperspectral microwave atmospheric sounding," *IEEE Trans. Geosci. Remote Sens.*, vol. 49, no. 1, pp. 128–142, Jan. 2011.
- [14] P. W. Rosenkranz, "Absorption of microwaves by atmospheric gases," *Atmospheric Remote Sensing by Microwave Radiometry*, vol. M. A. Janssen, Ed., Chapter 2, July 1993.
- [15] H. J. Liebe, "MPM: An atmospheric millimeter-wave propagation model," *International Journal of Infrared and Millimeter Waves*, vol. 10, no. 6, pp. 631–650, June 1989.
- [16] H. J. Liebe, P. W. Rosenkranz, and G. A. Hufford, "Atmospheric 60-GHz oxygen spectrum: New laboratory measurements and line parameters," *J. Quant. Spectrosc. Ra.*, vol. 48, Nov. 1992.
- [17] S.-P. Ho, et al., "Estimating the uncertainty of using GPS radio occultation data for climate monitoring: Inter-comparison of CHAMP refractivity climate records 2002–2006 from different data centers," *J. Geophys. Res.*, 2009.
- [18] S.-P. Ho, M. Goldberg, Y.-H. Kuo, C.-Z. Zou, and W. Schreiner, "Calibration of temperature in the lower stratosphere from microwave measurements using COSMIC radio occultation data: Preliminary results," *Terr. Atmos. Oceanic Sci.*, 2009.
- [19] S.-P. Ho, et al., "Reproducibility of GPS radio occultation data for climate monitoring: Profile-to-profile inter-comparison of CHAMP climate records 2002 to 2008 from six data centers," *J. Geophys. Res.*, 2012.
- [20] E. K. Smith and S. Weintraub, "The constants in the equation for atmospheric refractivity index at radio frequencies," *Proc. IRE*, pp. 1035–1037, 1953.
- [21] D. Thayer, "An improved equation for the radio refractive index of air," *Radio Sci.*, pp. 803–807, 1974.
- [22] J. A. Nelder and R. Mead, "A simplex method for function minimization," *Computer Journal*, vol. 7, pp. 308–313, 1965.
- [23] W. G. Read, Z. Shippony, and W. V. Snyder, *EOS MLS forward model algorithm theoretical basis document*. Pasadena, CA: Jet Propulsion Laboratory, 2003, available online: <http://swdev.jpl.nasa.gov/doc.htm#ATBDs>.



William J. Blackwell (S'92–M'02–SM'07) received the B.E.E. degree in electrical engineering from the Georgia Institute of Technology, Atlanta, GA, in 1994 and the S.M. and Sc.D. degrees in electrical engineering and computer science from the Massachusetts Institute of Technology (MIT), Cambridge, MA, in 1995 and 2002. Since 2002, he has worked at MIT Lincoln Laboratory, where he is currently an Assistant Leader of the Sensor Technology and System Applications group. His primary research interests are in the area of atmospheric remote sensing, including the development and calibration of airborne and spaceborne microwave and hyperspectral infrared sensors, the retrieval of geophysical products from remote radiance measurements, and the application of electromagnetic, signal processing and estimation theory. Dr. Blackwell held a National Science Foundation Graduate Research Fellowship from 1994 to 1997 and is a member of Tau Beta Pi, Eta Kappa Nu, Phi Kappa Phi, Sigma Xi, the American Meteorological Society, the American Geophysical Union, and Commission F of the International Union of Radio Science. He is currently an Associate Editor of the IEEE Transactions on Geoscience and Remote Sensing and the IEEE GRSS Magazine. He is Chair of the IEEE GRSS Frequency Allocations for Remote Sensing (FARS) technical committee, the IEEE GRSS Remote Sensing Instruments and Technologies for Small Satellites working group, and the Boston Section of the IEEE GRSS and serves on the NASA AIRS and NPP science teams, the JPSS Sounding Operational Algorithm Team, and the National Academy of Sciences Committee on Radio Frequencies. He is the Principal Investigator on the MicroMAS (Micro-sized Microwave Atmospheric Satellite) program, comprising a high-performance passive microwave spectrometer hosted on a 3U CubeSat planned for launch in 2013 and the Microwave Radiometer Technology Acceleration (MiRaTA) CubeSat planned for launch in 2015. He was previously the Integrated Program Office Sensor Scientist for the Advanced Technology Microwave Sounder on the Suomi National Polar Partnership launched in 2011 and the Atmospheric Algorithm Development Team Leader for the NPOESS Microwave Imager/Sounder. Dr. Blackwell received the 2009 NOAA David Johnson Award for his work in neural network retrievals and microwave calibration and is co-author of *Neural Networks in Atmospheric Remote Sensing*, published by Artech House in 2009. He received a poster award at the 12th Specialist Meeting on Microwave Radiometry and Remote Sensing of the Environment in March 2012 for "Design and Analysis of a Hyperspectral Microwave Receiver Subsystem" and was selected as a 2012 recipient of the IEEE Region 1 Managerial Excellence in an Engineering Organization Award "for outstanding leadership of the multi-disciplinary technical team developing innovative future microwave remote sensing systems."



Kerri Cahoy (S'00–M'08) received a B.S. in Electrical Engineering from Cornell University in 2000, an M.S. in Electrical Engineering from Stanford University in 2002, and a Ph.D. in Electrical Engineering from Stanford University in 2008. After working as a Senior Payload and Communication Sciences Engineer at Space Systems Loral, she completed a NASA Postdoctoral Program Fellowship at NASA Ames Research Center and held a research staff appointment with MIT/NASA Goddard Space Flight Center. She is currently a Boeing Assistant

Professor in the MIT Department of Aeronautics and Astronautics with a joint appointment in the Department of Earth and Planetary Sciences at MIT.



Pratik Dave received a B.S. in Aerospace Engineering from the University of Maryland in 2009. He has since been working at MIT Lincoln Laboratory as assistant research staff in the area of space systems analysis, and is currently pursuing an S.M. degree in Aeronautics and Astronautics from MIT as a Lincoln Scholar.